



Cite this: *Phys. Chem. Chem. Phys.*,  
2024, 26, 6216

# The sensitive aspects of modelling polymer–ceramic composite solid-state electrolytes using molecular dynamics simulations†

Melania Kozdra, <sup>a</sup> Daniel Brandell, <sup>a</sup> C. Moyses Araujo<sup>bc</sup> and Amber Mace <sup>\*a</sup>

Solid-state composite electrolytes have arisen as one of the most promising materials classes for next-generation Li-ion battery technology. These composites mix ceramic and solid-polymer ion conductors with the aim of combining the advantages of each material. The ion-transport mechanisms within such materials, however, remain elusive. This knowledge gap can to a large part be attributed to difficulties in studying processes at the ceramic–polymer interface, which are expected to play a major role in the overall ion transport through the electrolyte. Computational efforts have the potential of providing significant insight into these processes. One of the main challenges to overcome is then to understand how a sufficiently robust model can be constructed in order to provide reliable results. To this end, a series of molecular dynamics simulations are here carried out with a variation of certain structural (surface termination and polymer length) and pair potential (van der Waals parameters and partial charges) models of the  $\text{Li}_7\text{La}_3\text{Zr}_2\text{O}_{12}$  (LLZO) poly(ethylene oxide) (PEO) system, in order to test how sensitive the outcome is to each variation. The study shows that the static and dynamic properties of Li-ion are significantly affected by van der Waals parameters as well as the surface terminations, while the thickness of the interfacial region – where the structure–dynamic properties are different as compared to the bulk-like regime – is the same irrespective of the simulation setup.

Received 22nd September 2023,  
Accepted 2nd January 2024

DOI: 10.1039/d3cp04617f

rsc.li/pccp

## 1 Introduction

In recent years, solid-state electrolytes have attracted much attention for battery applications due to possible benefits when compared to the currently used liquid electrolytes.<sup>1</sup> Both polymer and ceramic solid electrolytes are possible candidates for use in this context. However, both these categories of materials, when used as a single phase, display drawbacks in terms of either electrochemical stability,  $\text{Li}^+$  conductivity, mechanical properties or interfacial compatibility. Since ceramic and polymer electrolytes have complementary advantageous characteristics, it is therefore frequently suggested that composites – produced by embedding conductive ceramic particles in a polymer matrix – could constitute a promising strategy to obtain the benefits of both material types.<sup>2</sup>

Although considerable attention has been dedicated to studying the performance and  $\text{Li}^+$  transport phenomena in such composite solid-state electrolytes, scientific literature

display plenty of contradictory findings and hypotheses concerning the  $\text{Li}^+$  transport mechanisms. On the one hand, some experimental studies show a decrease in  $\text{Li}^+$  conductivity in the composite material compared to a single polymer phase electrolyte, such as has been observed for garnet  $\text{Li}_7\text{La}_3\text{Zr}_2\text{O}_{12}$  (LLZO) combined with poly(ethylene oxide) (PEO).<sup>3,4</sup> On the other hand, other studies show an increase of conductivity when these two electrolyte materials are combined.<sup>5,6</sup> Such opposing results demonstrate that the true nature of  $\text{Li}^+$  transport in a composite electrolyte system remains elusive. For many composites, it is unclear which is the main ion-conducting phase: the polymer or the ceramic. Moreover, what is the interplay between the solid polymer electrolyte (SPE) salt and the ceramic particles? And is a space-charge region formed between the two electrolyte phases, and how important is it for the  $\text{Li}^+$  conduction?

There are several hypotheses in the field that address the questions listed above. Concerning the role of the salt, it has been suggested that the presence of ceramic particles induces adsorption of anions at the surface, which generates an improved ion–ion separation and thereby a higher cationic conductivity.<sup>7</sup> Another suggestion is that continuous conduction pathways through the ceramic phase are formed, especially at higher particle loadings. An active ceramic filler is often a

<sup>a</sup> Department of Chemistry – Ångström Laboratory, Uppsala University, Box 538, 75121 Uppsala, Sweden. E-mail: amber.mace@kemi.uu.se

<sup>b</sup> Department of Engineering and Physics, Karlstad University, Karlstad, Sweden

<sup>c</sup> Department of Physics and Astronomy, Materials Theory Division, Uppsala University, Box 516, 75120 Uppsala, Sweden

† Electronic supplementary information (ESI) available. See DOI: <https://doi.org/10.1039/d3cp04617f>



better ionic conductor in comparison to a solid polymer electrolyte, and can thereby render high overall conductivity.<sup>8</sup> Moreover, Li *et al.*<sup>9</sup> proposed a possible scenario in which a network of connected space-charge regions is formed at the surface of the LLZO ceramic. That creates fast conduction pathways at the ceramic surfaces. In contrast, Zagórski *et al.*<sup>4</sup> argued that LLZO micro-fillers do not contribute positively to the transport of Li<sup>+</sup> when embedded in the PEO polymer matrix. The presence of the ceramic active filler was shown to slow down the polymer chain mobility, resulting in a decrease in conductivity which is dominated by the polymer segmental motions. Thus, it remains unclear if lithium ions are transported within the ceramic phase, solely in the polymer phase, or along the ceramic–polymer interfaces, and if the addition of ceramic improves the conductivity or not.

The broad spectrum of proposed mechanisms of Li<sup>+</sup> transport in composite electrolytes illustrates the complexity of the problem at hand and is, in the literature, discussed in a wide range of composite electrolyte compositions, spanning from the ceramic-in-polymer to polymer-in-ceramic extremes.<sup>10</sup> This variation depends on the content of polymer and ceramic phases where the Li<sup>+</sup> transport pathways typically depend on the specific composition. Furthermore, there are many materials properties that may also affect the Li<sup>+</sup> mobility; for example, particle size,<sup>11,12</sup> ceramic phase morphology<sup>13,14</sup> or salt concentration<sup>15</sup> which makes it troublesome to compare results between studies and draw general conclusions, even for the most studied composite electrolyte system: LLZO/PEO. This material comprises garnet LLZO ceramic particles immersed in a PEO polymer matrix, and is the composite model system also considered in the present study. In order to obtain better insight into the dynamical and structural properties at the interface of LLZO and PEO materials, classical molecular dynamics (MD) methodology is employed. MD simulations can provide atomistic insights that are not directly accessible by the experiment, while they can resolve structure–dynamic properties which are difficult to assess with other simulation techniques.

The atomistic level MD simulations entail a length scale of the composite interphase that is too limited to differentiate into any specific composite electrolyte composition. However, understanding the behavior of Li<sup>+</sup> where the ceramic and polymer meet becomes mainly important for the ceramic-in-polymer electrolyte composition because transport across and along this interphase is expected to be dominant and rate-limiting. In the polymer-in-ceramic composition, the ions are anticipated to primarily transport along the ceramic phase and along/across the ceramic–ceramic interphase instead.

The aim of this work is to gain more understanding about the importance of different MD parameters when constructing a model of PEO/LLZO interfaces by determining how and to what extent different simulation setups affect the results. While this composite system has been examined by means of MD simulations in the past,<sup>16,17</sup> the effects of crucial simulation parameters have not yet been explored. The focus of this work thereby differs from previous studies; here we explore how sensitive the simulation outcome is to the choice of these specific simulation model

parameters. This will provide us with important information on which parts of the model are the weakest links, which input parameters need to be provided with the highest accuracy and which are less sensitive to change. In this study, the focus is specifically on how the MD simulation outcome is affected by changes of partial charges on atoms, van der Waals (vdW) cross interactions between polymer and ceramic, polymer chain length and surface termination. These offer valuable guidelines on how we can direct our research efforts most efficiently when further developing and improving the model accuracy of structure–dynamic processes that control the ionic transport. The primary focus of this study is thus to establish the foundation for conducting reliable and reproducible MD simulations of composite electrolytes rather than specifically providing a description of ionic transport phenomena at the current stage.

The choice of studied simulation parameters is divided into two categories: force field and structurally related aspects. vdW parameters together with partial charges belong to the first category. We use vdW parameters that have previously not been specifically optimised to describe the interfacial interactions between the ceramic and polymer phases. These sets of parameters have originally been developed to account for the interactions in a bulk material, and it is not yet clear if these interactions are compatible with an interfacial system. To our knowledge, there are no specifically optimised vdW parameters to account for cross-interactions between PEO and LLZO, or any other similar composite electrolyte systems.

Given that Li<sup>+</sup> interacts *via* vdW and Coulomb interactions, it is a natural choice to evaluate the importance of partial charges on the atoms. Atomic partial charge is an artificial concept, and there are many diverse methods to estimate these values. Thereby, we have used two sets of partial charges: (1) DDEC6 (abbreviated DDEC) charges computed based on atomic population analysis<sup>18</sup> and (2) REPEAT charges, which are derived from the electrostatic potential.<sup>19</sup> In addition, we used one set of charges that were employed in the past to simulate the LLZO material.<sup>20</sup>

Structurally related aspects are considered by studying the influence of the polymer chain length and surface termination on the simulation outcomes. The polymer chain length affects both polymer flexibility and the number of termination groups present. Surface–polymer interactions affect the polymer flexibility directly, and therefore ionic transport in the polymer. Moreover, the terminal group can significantly influence the coordination chemistry at the surfaces, and comparing simulations with different polymer chain lengths should therefore bring valuable insights about the model systems. Finally, the surface properties are known to significantly modify the interactions between two phases. Hence, we study the effect of surface termination while keeping the orientation constant.

## 2 Methods

### 2.1 Simulation box setup

The cubic LLZO structure was obtained from the ICSD crystallographic database.<sup>21</sup> In the LLZO crystal, there exists two types



of Li sites, 24 d and 96 h, that are partially occupied, with the respective occupation numbers 0.542 and 0.448.<sup>22</sup> Taking this into account, we generated an initial LLZO geometry that contained 13 and 43 Li atoms per unit cell in the 24 d and 96 h Li sites, respectively. This was done by randomly distributing these numbers of Li atoms among the specific site types. The initial slab configuration was generated using the Pymatgen “surface” module.<sup>23,24</sup> The slab was chosen to have a (100) orientation and a c-shift equal to 0.09 (as defined in the SlabGenerator class in Pymatgen), according to the surface energy analysis by Thompson *et al.*<sup>25</sup> Thereafter, a  $3 \times 3 \times 3$  LLZO slab was generated that was used in all simulations. Next, *fftool*<sup>26</sup> was used to assign partial charges to LLZO atoms and create a LAMMPS data file that was then used to generate the polymer–ceramic interface. In order to generate initial polymer coordinates and assign simulation parameters, the Enhanced Monte Carlo code<sup>27</sup> was used. This tool allows generating the polymer phase with different polymer chain lengths. The z-axis was chosen to be the axis perpendicular to the LLZO surface. This was then used to create a large enough box that contains both LLZO and PEO phases using the Moltemplate package.<sup>28</sup> All necessary details related to the simulation boxes, together with the system acronyms used throughout the text, are listed in Table 1. An example simulation box of the PEO:LiTFSI/LLZO interface is presented in Fig. 1. Finally, these initial geometries described in Table 1 were subjected to a thorough equilibration procedure. Due to the structural asymmetry in the z-direction, the construction of the slab generates two different surfaces: one terminated with oxygen and one terminated with lithium. Those are referred to as the left LLZO surface oxygen-terminated (L-LLZO) and right LLZO surface lithium-terminated (R-LLZO), respectively. The effects of this is dealt with in more detail in Section 3.2.1.

## 2.2 Equilibration and production run details

The LAMMPS package<sup>29</sup> was employed to perform all molecular dynamics simulations using periodic boundary conditions. To describe bonded interactions in the PEO polymer, the OPLS-AA<sup>30</sup> force field as defined in the enhanced Monte Carlo<sup>27</sup> software was used. Parameters for the TFSI<sup>−</sup> anions were adopted from Lopes *et al.*<sup>31</sup> The bond, angle and improper interactions were set as the harmonic style while dihedral interactions were multi/harmonic. The cutoff for all non-bonded interactions was equal to 12 Å. The non-bonded interactions of PEO and LiTFSI salt were described with Lennard-Jones (LJ) and Coulomb potentials. van der Waals interactions within the LLZO phase were described by a Buckingham

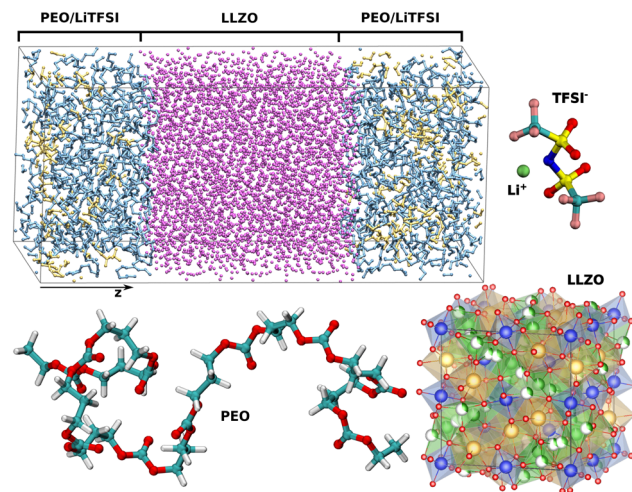


Fig. 1 Individual components present in the system: PEO, cubic LLZO, LiTFSI and an example of the simulation box. In the LLZO crystal: red, blue, green and yellow spheres represent O<sub>LLZO</sub>, Zr, Li<sub>LLZO</sub><sup>+</sup> and La atoms, respectively. In PEO and LiTFSI: red, cyan, white, dark blue, yellow and pink spheres represent O<sub>PEO</sub>, C, H, N, S and F, respectively. In the simulation box, all of the atoms in the ceramic phase are purple, all of the polymer atoms are blue with hydrogen atoms omitted for clarity and all of the LiTFSI atoms are yellow.

potential with parameters determined by Jalem *et al.*<sup>20</sup> Due to the lack of explicitly calculated parameters for cross interactions between the polymer phase and the LLZO ceramic, two sets of LJ parameters were tested for the LLZO atoms: universal force field (UFF) and another set consisting of Li<sup>+</sup> parameters from Wu *et al.*,<sup>32</sup> Zr and O from Martins *et al.*,<sup>33</sup> while the rest of the parameters were the same as in the UFF parameter set. This set is referred to as vdW-LiZrO in this paper. Since all atoms have associated LJ parameters, this allowed us to use Lorentz-Bertheloth mixing rules for interactions between non-identical atom pairs. Electrostatic interactions were modeled by performing a standard Ewald summation as implemented in LAMMPS, and fixed partial charges were assigned to all atoms in the system. The partial charges for LLZO and PEO atoms were obtained using the DDEC6<sup>18</sup> and REPEAT<sup>19</sup> methods; see Section S5 of the ESI† for details.

To equilibrate the composite systems, a 21 step procedure was followed according to the approach by Larsen *et al.*,<sup>34</sup> with the exception that the last NPT equilibration was extended to 32 ns. We used the last 2 ns of the final NPT to extract possible structures (every 10 ps) for the production NVT simulation. This was done in order to start the NVT simulation with the volume

Table 1 System descriptions

System name	Li:EO	No. chains	No. units	x, y [Å]	z [Å]	Density [g cm <sup>−3</sup> ]	vdW force field	Partial charges PEO	Partial charges LLZO
DDEC	—	1	900	39.26	83.25	2.91	UFF	DDEC	DDEC
REPEAT, LONG	—	1	900	38.87	80.04	3.09	UFF	REPEAT	REPEAT
OX	—	1	900	38.65	80.36	3.11	UFF	REPEAT	OX
SHORT	—	45	20	38.86	83.47	3.00	UFF	REPEAT	REPEAT
SHORT:LiTFSI	1:20	45	20	38.85	90.59	3.00	UFF	REPEAT	REPEAT
LONG:LiTFSI, vdW-UFF	1:20	1	900	38.86	87.25	2.90	UFF	REPEAT	REPEAT
vdW-LiZrO	1:20	1	900	38.87	86.51	3.02	vdW-LiZrO	REPEAT	REPEAT



as close as possible to the equilibrium value extracted from the final NPT simulation. Hydrogen's atomic mass was substituted with the mass of a deuterium atom, while all simulations were run with a time step of 1 fs. Temperature and pressure were maintained using a Nosé–Hoover thermostat and barostat as defined in LAMMPS. After the 21 step equilibration process, NVT simulations were run at 400 K for a duration of 500 ns. 499 ns was used for analysis of the properties in the system.

### 2.3 Analysis of atom distribution and Li<sup>+</sup> mobility

In order to have an initial look at the structural behavior of different atom types at the interface, number density profiles  $\rho(z)$  were calculated. First, the LLZO center of geometry was placed in the middle of the box. Next, a trajectory snapshot was obtained every 50 ps, and the positions of selected atoms were placed in bins with a thickness of 0.05 Å. The number density was plotted as a function of the  $z$  coordinate (perpendicular to the LLZO surface). Lastly, the average number of atoms per bin was divided by the volume of the 3D bin. Additionally, charge density profiles were calculated using the following equation,

$$q_{\text{tot}}(z) = \sum_{i=1}^N q_i \rho_i(z), \quad (1)$$

where  $N$  is the number of atoms in the system,  $q_i$  is the partial charge assigned to the  $i$ th atom and  $\rho_i(z)$  is the number density of the  $i$ th atom at position  $z$ . All density and charge profiles were centered on the LLZO phase and the crystal structure characteristics were clearly distinguishable from the polymer phase as sharp and distinct peaks.

The survival probability  $R(t)$  was calculated in order to obtain insight into the mobility of Li<sup>+</sup> in the direction perpendicular to the LLZO surface. This was calculated by,

$$R(t) = \frac{1}{T} \sum_{t=1}^T \frac{N(t, t + \tau)}{N(t)} \quad (2)$$

where  $T$  is the total number of time steps included,  $N(t)$  is the

number of particles that are found in the virtual bin at time  $t$  and  $N(t, t + \tau)$  is the number of particles that remains in that bin over the time span from  $t$  to  $t + \tau$ . By definition, the survival probability indicates how likely it is that a particle remains within a fictitious layer in a given time span; details are described by Liu *et al.*<sup>35</sup>

The box was divided in 4.5 Å thick virtual bins with zero being at the center of the simulation box, which is also the center of LLZO. In this way, a symmetric description of the two LLZO surfaces is obtained. The calculations of  $R(t)$  were performed every 5 ns to obtain satisfactory statistics. The survival probability, as defined by Liu *et al.*,<sup>35</sup> thereby contains all the history of a particle remaining in the respective artificial layer. It should be noted that fluctuations that may happen within 5 ps are ignored, *e.g.* if an atom travels out from and back into the layer within 5 ps, this is not detected.

It is worth noting that the survival probabilities can be used to estimate the Li<sup>+</sup> diffusion coefficient parallel to the slab, as described by Liu *et al.*<sup>35</sup> This method has been used in a recent study on a similar system.<sup>16</sup> The mean square displacement functions used to calculate the parallel diffusion coefficient with this method are themselves calculated from the Li<sup>+</sup> that remain in a fictitious layer, as defined for the calculation of the corresponding  $R(t)$ . However, in our simulations the Li<sup>+</sup> ions leave the fictitious layers before diffusive behavior is observed. For that reason, this method could not here be rigorously used to determine the parallel diffusion coefficients, but only for qualitative indications for comparative purposes (the calculated MSDs from our trajectories that did not reach the diffusive regime are not reported here).

## 3 Results and discussion

### 3.1 General observations of the structure–dynamic properties

**3.1.1 Common features in density profiles.** Fig. 2 displays the total density profiles of O<sub>PEO</sub>, O<sub>TFSI</sub><sup>−</sup> and Li<sub>PEO</sub><sup>+</sup>, which gives a direct indication on how the atoms are structurally organized

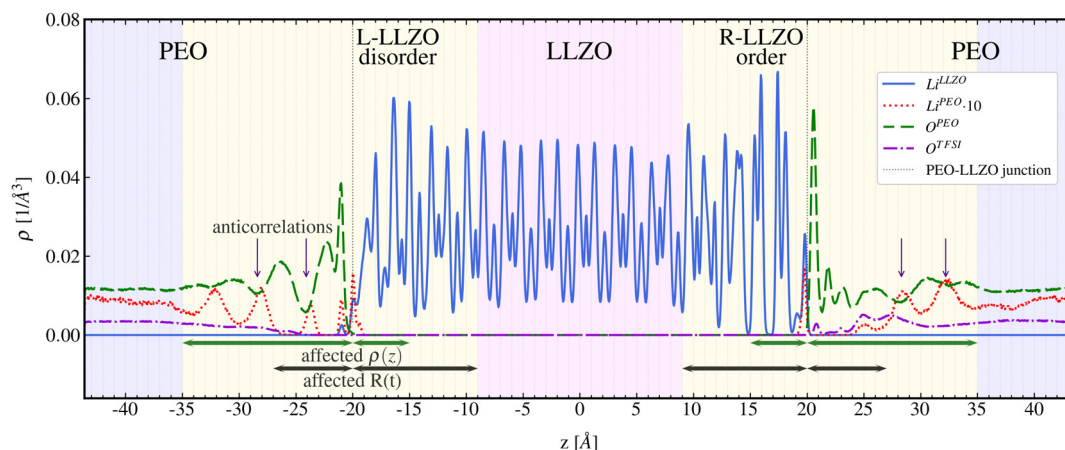


**Fig. 2** Atom number density profiles of the LONG:LiTFSI system  $\rho(z)$  centered around the LLZO phase. The ordered (less mobile) and disordered (more flexible) areas are indicated with 5 Å thick green arrows. While the green arrows indicate the region in which  $\rho(z)$  are affected by the presence of the LLZO surface, the black arrows indicate the regions in which the survival probability  $R(t)$  is affected.





in the  $z$ -direction of the simulation cell. The LLZO phase is centered around  $z = 0$ , extending to *ca.*  $z = \pm 20$  Å, where the sharp peaks indicate the expected layered structure, while the polymer electrolyte occupies the region beyond  $z = \pm 20$  Å. As shown by the liquid-like signature peaks that indicate ordering in the polymer phase, the presence of ceramic surfaces significantly affects the distribution of  $O_{\text{PEO}}$  up to about 15 Å from both L-LLZO and R-LLZO surfaces. This effect fades away above 15 Å and the structural properties become more bulk-like. The regions within the intervals  $z = [\pm 35, \pm 20]$  Å, constitute an “interphase” region being formed within the simulation time, with structural properties different than in the bulk. In all systems with LiTFSI salt present in the PEO phase, a negative correlation between  $\text{Li}_{\text{PEO}}^+$  and  $O_{\text{PEO}}$  intensities is observed. In other words, the density profiles of  $\text{Li}_{\text{PEO}}^+$  show maxima at positions that correspond to the minima of  $O_{\text{PEO}}$  in the interfacial region; this is indicated in Fig. 2. This means that in the polymer part of the interphase,  $\text{Li}_{\text{PEO}}^+$  ions prefer to reside in areas of lower  $O_{\text{PEO}}$  mass density and it is significantly less probable to find  $\text{Li}^+$  in regions of higher  $O_{\text{PEO}}$  density. It is worth noting that in all simulations that contain LiTFSI salt in the polymer phase, accumulation of  $\text{Li}_{\text{PEO}}^+$  ions at the L-LLZO surface can be observed, which means that the PEO phase is depleted from  $\text{Li}^+$ . This structurization into layer-like accumulation of ionic species and polymers close to surfaces have been observed in previous simulations of SPE materials on Li-metal<sup>36</sup> and graphene.<sup>37</sup>

**3.1.2 Distribution of TFSI<sup>−</sup> anions.** The distribution of TFSI<sup>−</sup> shows a  $\sim 4$  Å thick depletion region at the L-LLZO surface, while at the R-LLZO side the anion peaks are directly adhering to the ceramic surface. Not only can a closer proximity to the R-LLZO surface of the TFSI<sup>−</sup> ions be observed, but also a higher anion density at that side of the ceramic phase. This accumulation of negatively charged TFSI<sup>−</sup> ions at the R-LLZO surface is consistent with the fact that R-LLZO has a higher positive charge compared to L-LLZO, as discussed in Section 3.2.1. In previous work on similar systems, this depletion region around the LLZO surfaces was only observed for the cation. The difference in surface terminations, which is not specified in previous work,<sup>16</sup> may be responsible for these differences.

**3.1.3 Li<sup>+</sup> density distribution at the LLZO surfaces.** Bonilla *et al.*<sup>16,17</sup> noted an amorphous  $\text{Li}_{\text{LLZO}}^+$  layer *ca.* 4 Å thick being formed at both L-LLZO and R-LLZO surfaces. Our results do not appear to corroborate this observation; such a layer is here only observed at the L-LLZO side of the slab, while the R-LLZO side is characterised by more ordered and rigid  $\text{Li}_{\text{LLZO}}^+$  positions. It could possibly be hypothesized that this difference is due to the LLZO force field parameters used in the respective simulations. However, when using the same partial charges and vdW parameters to describe LLZO atoms as Bonilla *et al.* (as in the OX system), the same discrepancies between the L-LLZO and R-LLZO atom distributions appear. Therefore, these differences can instead rather be explained by the LLZO slab terminations. Moreover, these previous studies have employed an LLZO structure doped with Ga atoms, which have not been done here.

**3.1.4 Interfacial effects on Li<sup>+</sup> survival probabilities.** The survival probability of  $\text{Li}^+$  for all systems is plotted in Fig. 3. This property indicates the timescales of  $\text{Li}^+$  transport perpendicular to the LLZO surfaces. A rapidly decaying  $R(t)$  corresponds to fast ionic transport in the  $z$ -direction. The  $R(t)$  plots close to the interface demonstrate that transport perpendicular to the surface is affected in the region spanning  $[\pm 9, \pm 27]$  Å, where the  $R(t)$  functions decay much slower than in the regions  $[0, \pm 9]$  Å and  $[\pm 27, \pm 36]$  Å, which contain ceramic and polymer bulk-like phases, respectively. This means that the presence of the PEO phase (or just the fact that there is a surface introduced) affects  $\text{Li}_{\text{LLZO}}^+$  mobility in the LLZO material up to about 11 Å from the surface. In a similar way, the perpendicular mobility of  $\text{Li}_{\text{PEO}}^+$  in the polymer phase is affected up to about 7 Å from the surface, regardless of the system setup. Also these results suggest that the interphase region spans the region  $[\pm 9.0, \pm 27.0]$  Å in the simulation box, considering that it is the distance where the survival probability of  $\text{Li}^+$  in both ceramic and polymer deviate from the properties of the bulk-like layers.

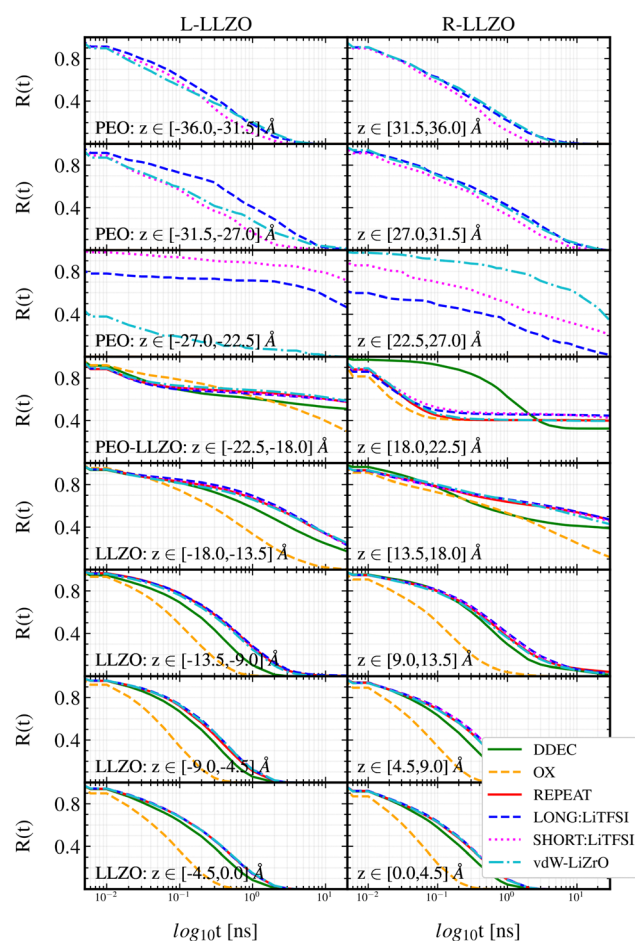


Fig. 3 Survival probability functions. The different boxes correspond to different segments in the simulation box, with the respective  $z$ -values stated in each box. The bottom boxes thereby represent the bulk of the LLZO phase, while the top represents the bulk of the polymer phase (acronyms in the legend are explained in Table 1).



Moreover, the general trends for all systems, and for both LLZO surfaces, are that the survival probability decays the fastest  $\sim 10^0$  ns in layers that are in the center of the LLZO ceramic  $[0.0, \pm 9.0]$  Å. From Fig. 3 it can be seen that 50% of the  $\text{Li}^+$  moves out of the  $[0.0, \pm 4.5]$  and  $[\pm 4.5, \pm 9.0]$  layers within 1 ns, and after 1.1 ns all  $\text{Li}^+$  in a given fictitious layer have been exchanged for new ions. Next, in the interfacial region that spans both ceramic and polymer phases, *i.e.*  $[\pm 9.0, \pm 27.0]$  Å,  $R(t)$  gradually increases to be at its maximum  $> 10^1$  ns within the  $[\pm 18.0, \pm 27.0]$  Å region. This means that  $\text{Li}^+$  remains the longest time in this region. In other words, the presence of the interface hinders  $\text{Li}^+$  mobility perpendicular to the ceramic surface both in the polymer and ceramic phase. Lastly, towards the center of the polymer phase above/below  $\pm 27.0$  Å, the survival probability decays faster, similarly to the ceramic phase, reaching values at the level of  $\sim 10^1$  ns in all except the vdW-LiZrO system. This case will be discussed in more detail in Section 3.3.2.

**3.1.5 Common characteristics of the interfacial region.** A common feature for all systems is that the density profiles of species in the polymer phase are significantly affected by the presence of the interface up to about 15 Å from the surface, while in the ceramic phase this interfacial layer is about 5 Å thick. It is thereby clear that the density profiles show a thicker layer being affected in the polymer phase compared with in the ceramic phase. At the same time, the reversed situation (a thicker affected layer in the ceramic phase than in the polymer phase) takes place when the survival probability is studied; *i.e.*, the dynamic properties. A layer of only 7 Å in the SPE phase shows higher  $R(t)$  than the bulk, while in the LLZO this layer reaches about 11 Å; see Fig. 2 where these regions are indicated with black arrows.

## 3.2 Structural effects

**3.2.1 Surface terminations.** The main differences between the L-LLZO and R-LLZO surfaces can be analyzed for all simulated systems by studying the density profiles; the discussed areas (5 Å thick) are indicated with green arrows in Fig. 2. The analysis is here done based on the LONG:LiTFSI system (see Table 1), but these observations qualitatively correspond to the results observed also for the other systems.

*Surface effects on the  $\text{Li}^+$  density distribution.* In the initial input of the MD simulation, the L-LLZO surface is terminated with  $\text{O}_{\text{LLZO}}$  atoms. However, within the simulation time, mobile  $\text{Li}_{\text{LLZO}}^+$  ions populate the surface. Here, the  $\text{Li}_{\text{LLZO}}^+$  atom density at the surface is about  $0.01 \text{ Å}^{-3}$ , and the distance between this density peak and the first  $\text{O}_{\text{PEO}}$  maximum is about 1.2 Å; see Fig. 2. The polymer and LLZO phases on this side thereby seem to repel each other. Since the atom density of  $\text{Li}_{\text{LLZO}}^+$  is above zero everywhere in this region, there is a possibility of  $\text{Li}_{\text{LLZO}}^+$  changing between different LLZO layers, indicating disorder and flexibility. The R-LLZO surface, in turn, is initially terminated with  $\text{Li}_{\text{LLZO}}^+$  ions. At this surface the  $\text{Li}_{\text{LLZO}}^+$  atom density at the surface is almost three times the density of L-LLZO surface, *i.e.* almost  $0.03 \text{ Å}^{-3}$ , while the

distance between this peak and the first  $\text{O}_{\text{PEO}}$  maximum is only about 0.7 Å. This indicates a tighter adhesion of the polymer to the R-LLZO surface compared to the L-LLZO side, see Fig. 2. The interfacial  $\text{Li}_{\text{LLZO}}^+$  peaks on the R-LLZO side are also characterised by precise positions. Ion exchange between LLZO layers is therefore less likely, which indicates a higher level of ordering and rigidity compared to the L-LLZO surface. A common characteristic for both surfaces is that the interfacial  $\text{Li}_{\text{LLZO}}^+$  layers, except for the terminal ones, have noticeably higher atom density compared to the center of the LLZO phase. This means that  $\text{Li}_{\text{LLZO}}^+$  tend to accumulate near the surfaces within a region of *ca.*  $z = [\pm 15.0, \pm 18.0]$  Å, see Fig. 2.

*Surface effects on the  $\text{Li}^+$  mobility.* To further highlight the differences in ion exchange between LLZO layers at the two surfaces, the  $\text{Li}_{\text{LLZO}}^+$  trajectories (up to 4 Å from the surface) are displayed in Fig. 4. Indeed, the mobility of  $\text{Li}_{\text{LLZO}}^+$  ions is much higher at the L-LLZO side compared to the R-LLZO side. From the trajectories, it is observed that the L-LLZO surface atoms travel almost the entire interior of the LLZO phase while the R-LLZO surface atoms hardly move from their initial positions, hence the trajectory covers only a thin region around the R-LLZO surface.

*Surface effects on the charge distribution.* Qualitatively, the analysis of Zr, La,  $\text{O}_{\text{LLZO}}$  and  $\text{Li}_{\text{LLZO}}^+$  density profiles of L-LLZO and R-LLZO surfaces indicate that there is an increased accumulation of positively charged Zr and La close to the R-LLZO surface as compared to the L-LLZO surface. Moreover, these positive charges are shielded by negatively charged  $\text{O}_{\text{LLZO}}$  atoms to a lesser extent at R-LLZO than at L-LLZO. This suggests that the L-LLZO surface is more negatively charged than the R-LLZO surface, which can explain the differences in charge accumulation from the polymer phase.

**3.2.2 Polymer chain length.** The effect of polymer chain length can be directly studied by comparison of the systems SHORT:LiTFSI and LONG:LiTFSI (Table 1); for simplicity, they

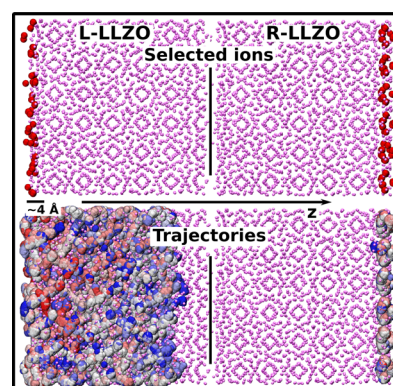


Fig. 4 Trajectories of  $\text{Li}_{\text{LLZO}}^+$  from the final 100 ns of simulation in the LONG:LiTFSI system at L-LLZO and R-LLZO surfaces.  $\text{Li}_{\text{LLZO}}^+$  atoms were selected at each surface spanning a 4 Å thick layer. Red, white and blue spheres indicate the beginning, middle and the end of the trajectory, respectively. The purple spheres indicate positions of all LLZO atoms at one snapshot.



are abbreviated as SHORT and LONG respectively in the following.

**Chain length effects on the TFSI<sup>−</sup> density distribution.** Interestingly, the interactions of anions with LLZO surfaces are affected by the difference in the polymer chain length. For example, the density profiles of the components of the LiTFSI salt show that the TFSI<sup>−</sup> ions are found closer by about 1 Å to both surfaces and the peaks have a higher intensity in the SHORT as compared to the LONG system; see Fig. 5. Concerning the system with short polymer chains, the TFSI<sup>−</sup> ions show a similar atom distribution at both sides of the LLZO slab in the regions  $z = [\pm 25.0, \pm 30.0]$  Å. This corresponds to an observed increase of anion density as compared to other areas in the simulation box. At the same time in the LONG system, there is a discrepancy in the atom distribution of TFSI<sup>−</sup> ions between the left and right side of the LLZO slab. At the L-LLZO surface, a decrease in TFSI<sup>−</sup> ions is observed in the region  $z = [-30.0, -25.0]$  Å while an increase is visible at the R-LLZO side at the corresponding distance from the surface. These observations are highlighted in the ESI,† Fig. S2, which shows the trajectories of  $N_{\text{TFSI}^-}$  atoms selected within 7 Å from the surface. Indeed, the TFSI<sup>−</sup> ions seem to populate larger regions perpendicular to the surface in the SHORT system as compared to the LONG system. Moreover, a TFSI<sup>−</sup>-free volume is found in the LONG simulation at the L-LLZO side, shown in the ESI,† Fig. S2. This means that there is a consistency between the ESI,† Fig. S2 and the  $N_{\text{TFSI}^-}$ -density profiles shown in Fig. 5a. As explained above, a decrease of TFSI<sup>−</sup> atom density is observed in the region  $z = [-30.0, -25.0]$  Å. There is a 4 and 5 Å thick anion depletion area, respectively, at the L-LLZO surface in both SHORT and LONG simulations.

These discrepancies between density profiles of the TFSI<sup>−</sup> ions in the LONG and SHORT systems may have a twofold explanation. First, it is possible that the distribution of the anions in the polymer phase has reached equilibrium in the

SHORT system but not in the LONG system. Simulations of a bulk PEO-LiTFSI system with short polymer chains (<100 monomers) show *ca.* 2.5 times faster diffusion of TFSI<sup>−</sup> in comparison to higher molecular weight polymer chains.<sup>38</sup> This indicates that the TFSI<sup>−</sup> density profiles of the SHORT system are more likely to be the equilibrium atom distribution, compared to the LONG system. However, the anion diffusive regime in the bulk PEO-LiTFSI simulations was reached within 400 ns, even in the simulations with the long polymer chains (>100 monomers).<sup>38</sup> Therefore, it seems that short and long polymer chains interact differently with the L-LLZO surface, which in turn affects the TFSI<sup>−</sup> ions distribution. The longer PEO chain creates a thicker shell around the L-LLZO surface in the LONG system compared to the SHORT system; see the  $O_{\text{PEO}}$  atom density plots in the ESI,† Fig. S6. The observed thinner and more permissible shell, that the shorter PEO chains form around the L-LLZO surface, is likely due to a higher chain flexibility. This results in a more accessible PEO interfacial shell for the TFSI<sup>−</sup> ions in the SHORT system as compared to the LONG system.

**Chain length effects on the Li<sup>+</sup> interphase penetration.** Another discrepancy between the interfacial atom distributions in the SHORT and LONG systems is that there is an uptake of  $\text{Li}_{\text{PEO}}^+$  ions into the LLZO slab only in the system with short polymer chains. Penetration of Li<sup>+</sup> occurs only through the L-LLZO surface and the ions do not cross the LLZO phase entirely. One example of a Li<sup>+</sup> ion entering the ceramic phase through the L-LLZO surface is shown in Fig. 6, which shows 300 ns of a trajectory of a  $\text{Li}_{\text{PEO}}^+$ . The highlighted Li<sup>+</sup> spends about 100 ns in each region: the polymer phase, at the interface and in the ceramic phase. Density profiles of  $\text{Li}_{\text{PEO}}^+$  in Fig. S6 in the ESI† show a more quantitative picture of  $\text{Li}_{\text{PEO}}^+$  entering the LLZO phase, while in the SHORT system the peaks in the LLZO phase (at  $z > -20$  Å) indicate the presence of  $\text{Li}_{\text{PEO}}^+$ . In the LONG system, no peaks are observed in the LLZO phase.

Despite the uptake of  $\text{Li}_{\text{PEO}}^+$  into the LLZO phase, which is observed in SHORT but not in the LONG simulations, the survival rate  $R(t)$  is not affected in the ceramic region  $[0.0, \pm 22.5]$  Å by the presence of additional Li<sup>+</sup> ions in the crystal structure; see Fig. 3. It is common for both polymer lengths for

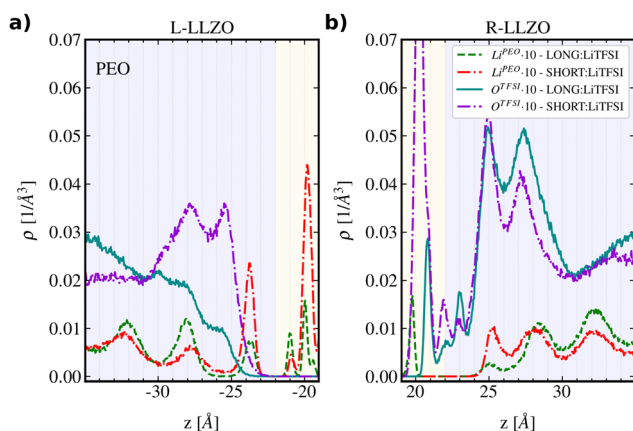


Fig. 5 Atom number density profiles  $\rho(z)$  centered around the LLZO phase. Comparison of results of the simulations with different polymer chain lengths, zoomed: (a) at the L-LLZO surface and (b) at the R-LLZO surface. The yellow background indicates the 4 Å (arbitrary thickness) interface region. Blue and purple backgrounds denote the PEO and LLZO phases, respectively.

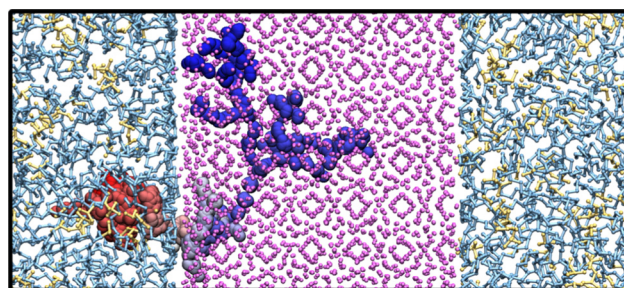


Fig. 6 Trajectories of a single Li<sup>+</sup> from the final 300 ns of simulation in the SHORT:LiTFSI system. Red, white and dark blue spheres indicate the beginning, middle and the end of the trajectory, respectively. Purple spheres indicate the extent of the LLZO phase, yellow and bright blue spheres and sticks indicate TFSI<sup>−</sup> and PEO respectively.





$\text{Li}_{\text{PEO}}^+$  ions to be adsorbed at the LLZO surfaces, but  $\text{Li}_{\text{LLZO}}^+$  do not leave the LLZO phase. Fig. S3 in the ESI† shows how the number of  $\text{Li}^+$  present in the LLZO phase and its surface ( $z$ -span  $[-22, 22]$  Å) evolves as a function of simulation time. Fig. S3 in the ESI† indicates that the process of  $\text{Li}_{\text{PEO}}^+$  uptake in the ceramic phase has not reached an equilibrium stage in any of the simulations, which is deduced from the fact that a stable plateau is not reached. By the end of the simulation time, the polymer phase contains 82% and 93% of the initial number of  $\text{Li}_{\text{PEO}}^+$  ions, in the SHORT and LONG systems respectively.

One possible explanation for the discrepancies between the long and short polymer chain simulations is that the ionic transport occurs faster in SHORT due to the increased chain flexibility. This would mean that the same  $\text{Li}^+$  and  $\text{TFSI}^-$  distribution will be reached in LONG if it was simulated for a longer time. However, the  $\text{Li}^+$  survival probability in the regions  $z = [\pm 22.5, \pm 27.0]$  Å, is higher in the system with shorter chains, which indicates that the cationic transport perpendicular to the surface occurs on a shorter timescale in the system with the long polymer chain. This is contrary to what would be expected given that in the simulations of a bulk PEO electrolyte, it was found that shorter polymer chains correlate with faster  $\text{Li}^+$  diffusion.<sup>38</sup> Although the  $\text{Li}_{\text{PEO}}^+$  remain longer in the region  $z = [\pm 22.5, \pm 27.0]$  Å in the SHORT system, they pass through it to reach the areas near the surfaces, as indicated in the ESI† Fig. S6. This corroborates with data in Fig. S3 in the ESI† which shows that more  $\text{Li}_{\text{PEO}}^+$  ions reach the LLZO surfaces in the SHORT system compared to the LONG system. These reasons indicate that polymer flexibility, and therefore the timescale of ion transport, may be a reason for discrepancy in the simulations.

**Polymer chain terminations.** Another difference between the systems is the number of polymer chain terminations, comprising 2 and 90 terminations in the LONG and SHORT systems, respectively. Although the chains in these simulations are terminated with relatively inert methyl groups, there is a difference in adhesion of  $\text{O}_{\text{PEO}}$  to the surfaces in the interfacial layers  $z = [\pm 20, \pm 27]$  Å.  $\text{O}_{\text{PEO}}$  density profiles in the ESI† Fig. S6, demonstrate this difference in the interfacial atoms arrangement that does not overlap for the SHORT and LONG systems respectively. 100 ns of trajectories of  $\text{C}_{\text{PEO}}^{\text{terminal}}$  atoms are shown in the ESI† Fig. S1. It is visible that terminations accumulate at the surface in SHORT while they remain at the center of the polymer phase in the LONG system. This could be a result of the difference in flexibility of the long and short polymer chains which may lead to a modification of the more likely polymer configuration at the surface. At the same time, the polymer chain length does not affect density profiles of  $\text{O}_{\text{PEO}}$  in systems without the salt in the polymer phase; see Fig. S5 in the ESI† This indicates that the presence of  $\text{LiTFSI}$  salt in the polymer phase, and possibly its interaction with chain terminations, has a more prominent effect on the interfacial  $\text{O}_{\text{PEO}}$  distribution than a difference in the polymer chain length alone.

### 3.3 Force field effects

**3.3.1 Partial charges.** In order to study the effect of partial charges, the atom number density and charge density profiles

of three systems were compared: OX, DDEC and REPEAT. The differences between these force fields are the magnitudes of charge assigned to each PEO, LLZO atom and  $\text{TFSI}^-$  atom. In general, the charge magnitude increases in the following order: DDEC, REPEAT and OX, Table S0 in the ESI† lists the exact values of the assigned charges to each atom in the system. In the ESI† Fig. S4, which displays the distribution of total charge in the  $z$  direction, it can be noticed that OX display more pronounced maxima and minima compared to DDEC and REPEAT systems. This indicates a higher spread of the charge density along the layers of LLZO and stronger electrostatic interactions. This result is in line with the fact that La and Zr possess a higher positive charge in the OX system compared to the other two, see Table S0 in the ESI†.

#### Charge effects on the polymer adhesion to the LLZO surface.

The interaction of  $\text{O}_{\text{PEO}}$  is stronger with the LLZO surface in OX and REPEAT compared to DDEC. This difference may be explained by analyzing the interactions of  $\text{O}_{\text{PEO}}$  with the cations of the LLZO phase; this is indicated in Fig. 7, which shows charge density distribution along the  $z$ -axis. The distance between the closest  $\text{O}_{\text{PEO}}$  and Zr peaks to the interface is about 3–4 Å. At that distance, the attraction energy between these species reaches about  $400 \text{ kJ mol}_{\text{pair}}^{-1}$  (*i.e.*, the sum of Coulomb and van der Waals pair interactions) in the OX and REPEAT systems, but only about  $180 \text{ kJ mol}_{\text{pair}}^{-1}$  in the DDEC system. Similarly, when the interaction energy of the  $\text{O}_{\text{PEO}}$ -La pair is studied, it can be noticed that the interaction energy reaches about  $250 \text{ kJ mol}_{\text{pair}}^{-1}$  and  $700 \text{ kJ mol}_{\text{pair}}^{-1}$  in DDEC and REPEAT/OX respectively, at the typical interfacial distance of 2.5 Å. This interaction energy analysis can explain the difference in polymer adhesion to the surface; *i.e.* that the REPEAT and OX have higher attractive interaction energies between the polymer and ceramic atoms compared to the DDEC system. This is consistent with weaker interactions between the phases in this system, which is seen in Fig. 7 by

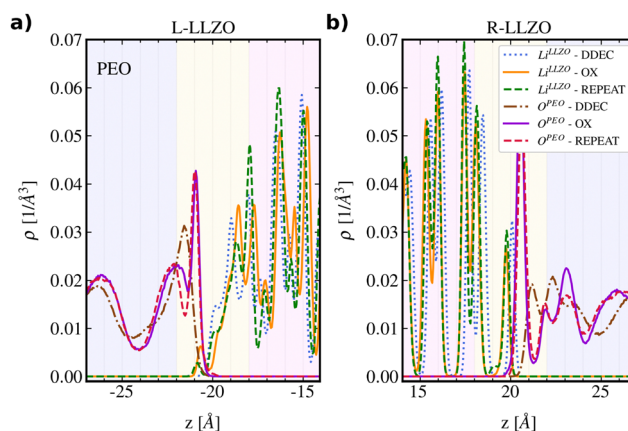


Fig. 7 Atom number density profiles  $\rho(z)$  centered around the LLZO phase. Comparison of the results of simulations with different partial charges on atoms, zoomed in: (a) at the L-LLZO surface and (b) at the R-LLZO surface. The yellow background indicates the 4 Å (arbitrary thickness) interface region. The blue and purple backgrounds are the PEO and LLZO phases respectively.





observing the distance and intensity of  $O_{\text{PEO}}$  and  $Li_{\text{LLZO}}^+$  interfacial peaks.

**Charge effects on the  $Li_{\text{LLZO}}^+ - O_{\text{PEO}}$  interactions.** Moreover, the character of the first  $O_{\text{PEO}}$  adhering layer is different in these systems. For example, in Fig. 7a at the region  $[-23, -21]$  Å, the DDEC system shows only one peak located slightly further from the surface, while in the other systems the first adhering layer is split into two peaks. In the OX and REPEAT systems, a small number of  $Li_{\text{LLZO}}^+$  are adsorbed to the first layer of the polymer at the L-LLZO side. The OX system is different from REPEAT only by the partial charges in the LLZO phase, while both systems have the same set of charges in the polymer phase. This effect is not observed in any of the systems at the R-LLZO side, neither is it observed on any side of LLZO in the DDEC system. The fact that we do not observe  $Li_{\text{LLZO}}^+$  migration towards the first PEO layer in the DDEC system may be explained by the interaction energies of  $Li^+$  ions with other atoms in the system. Due to the lower magnitude of partial charges, there is much lower attractive Coulomb interaction between the polymer atoms and  $Li^+$  in the DDEC system compared to the REPEAT system. For example, the  $Li^+ - O_{\text{PEO}}$  interactions at 2 Å is about  $110 \text{ kJ mol}_{\text{pair}}^{-1}$  and  $300 \text{ kJ mol}_{\text{pair}}^{-1}$  in the respective systems. At the same time, the interactions of  $Li^+$  with LLZO atoms are comparable for both systems. This means that the DDEC charges induce a weaker interaction of  $Li^+$  ions with the PEO atoms, which prevents the migration of  $Li_{\text{LLZO}}^+$  atoms towards the polymer phase.

**Charge effects on the  $Li^+$  mobility in the LLZO phase.** In Fig. 3, vital differences between the employed partial charges on the survival rates can be observed. The OX system shows about one order of magnitude faster decay of  $R(t)$  compared to both DDEC and REPEAT. The survival probability of  $Li^+$  in system OX varies between  $\sim 5 \times 10^{-1} \text{ ns}$  to  $\sim 1 \times 10^1 \text{ ns}$  in the regions  $[0.0, \pm 18.0]$  Å, while  $R(t)$  in systems DDEC and REPEAT is about one order of magnitude higher. A trend can be seen that the survival probability decays the slowest in the REPEAT system, while it is slightly faster in DDEC as compared to REPEAT. This observation is valid for both L-LLZO and R-LLZO sides. Despite the higher magnitude of charges in the OX system (which implies stronger Coulomb interactions between atoms), the  $Li_{\text{LLZO}}^+$  mobility perpendicular to the surface proceeds on shorter timescales in that system than in DDEC and REPEAT systems. It is not possible to directly pinpoint the exact reason for the discrepancies between these simulations due to the high number of pair interactions. However, the two possibly dominant interactions in LLZO, the Li-O and Li-Li pairs, may provide some insights. At about 2 Å (the typical distance between the nearest Li-O neighbours) the interaction energy in the OX system is  $50 \text{ kJ mol}_{\text{pair}}^{-1}$  and  $100 \text{ kJ mol}_{\text{pair}}^{-1}$  weaker (*i.e.*, lower attractive interaction) compared to DDEC and REPEAT systems respectively. The Li-Li repulsive pair interaction is the weakest in the OX system with a difference of at least  $80 \text{ kJ mol}_{\text{pair}}^{-1}$  compared to other systems. This means that there may be more flexibility for  $Li_{\text{LLZO}}^+$  in the LLZO structure, which therefore

leads to the higher mobility perpendicular to the surface in the OX system compared to other systems. This analysis is consistent with the work of Jalem *et al.*,<sup>39</sup> where it is shown that the unstable residence of  $Li_{\text{LLZO}}^+$  at the 24d site is one of the main factors for the fast concerted  $Li^+$  migration mechanism in cubic LLZO.

**3.3.2 van der Waals potentials.** In Fig. 8, the  $Li^+$  and  $O_{\text{PEO}}$  density profiles of vdW-LiZrO and vdW-UFF systems are compared. These force fields differ only by a few of the vdW cross interactions between the ceramic and the polymer atoms. Nevertheless, significant differences in the interfacial atom arrangements can be seen, which are distinctively reflected in the density profiles at the LLZO surfaces.

**Force field effects on the  $Li^+$  depletion region.** A first observation from the  $Li^+$  density distribution is that in the vdW-UFF system at the L-LLZO surface  $[-25.0, -18.0]$  Å, there are three peaks corresponding to the most probable positions of  $Li_{\text{PEO}}^+$ , while in vdW-LiZrO only two peaks are observed. In other words, a  $\sim 4$  Å thick depletion region of  $Li_{\text{PEO}}^+$  species appear in vdW-LiZrO but not in the vdW-UFF simulation; see the  $[-26.0, -22.0]$  Å region in Fig. 8a. This kind of depletion region is also observed in both systems at the R-LLZO surface, and has also been noted in previous atomistic simulation of the same system.<sup>16</sup> Additionally, changing cross vdW parameters affects the intensities and positions of several maxima and minima in the interfacial region of the density profiles of  $Li_{\text{LLZO}}^+$  on both surface sides, which is seen when comparing the  $Li_{\text{LLZO}}^+$  peak positions in Fig. 8.

**Force field effects on the adhesion of  $O_{\text{PEO}}$  to the LLZO surfaces.** The character of the interfacial  $O_{\text{PEO}}$  peaks is also visibly affected by the change of vdW parameters. There is one minimum less, and some maxima are also shifted or have higher/lower intensity in the vdW-LiZrO system compared to the vdW-UFF system. In Fig. 8a, it can be noted that adhesion of  $O_{\text{PEO}}$  is

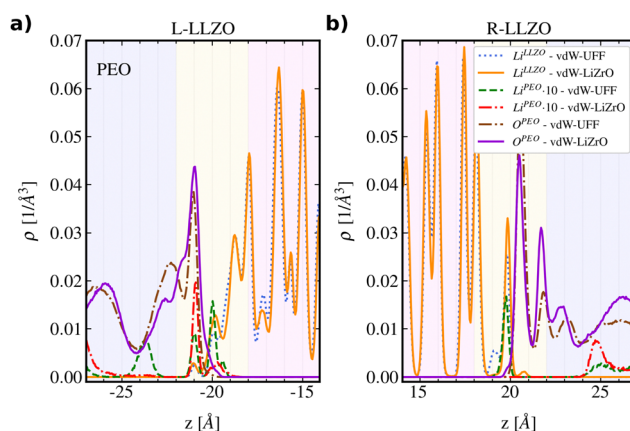


**Fig. 8** Atom number density profiles  $\rho(z)$  centered around the LLZO phase. Comparison of results of the simulations with different vdW cross parameters, zoomed in: (a) at the L-LLZO surface and (b) at the R-LLZO surface. The yellow background indicates the 4 Å (arbitrary thickness) interface region. Blue and purple background are the PEO and LLZO phase respectively.



stronger in vdW-LiZrO compared to vdW-UFF (see the brown-dashed and violet-solid lines, respectively). The above analysis suggests that modification of the vdW cross parameters affects the arrangement of interfacial  $O_{\text{PEO}}$  which may induce a  $\text{Li}_{\text{PEO}}^+$  depletion region at the L-LLZO interface. Furthermore, adhesion of  $O_{\text{PEO}}$  to the R-LLZO surface is stronger compared to L-LLZO in the vdW-UFF system, while in vdW-LiZrO  $O_{\text{PEO}}$  adhesion on both surface sites is comparable. These results indicate that the choice of vdW parameters affects adhesion of  $O_{\text{PEO}}$  differently depending on the surface terminating atoms. This can be rationalised by the fact that different LLZO terminations have different electrostatic interactions, *i.e.* that the atoms possessing the same charge will be exposed to different Coulomb interaction regions when the vdW parameters are modified.

**Force field effects on the  $\text{Li}^+$  survival probabilities.** The effect of vdW parameters on the survival probability  $R(t)$  is most pronounced in the regions  $[\pm 22.5, \pm 27.0]$  Å (Fig. 3). In particular, the vdW-LiZrO system shows the fastest decay of all systems at the L-LLZO side. Concerning R-LLZO, the opposite situation takes place with the vdW-LiZrO system showing slower  $R(t)$  decay when compared to the vdW-UFF system. The vdW-LiZrO system shows a significantly faster decay of the survival probability in the region  $[-27.0, -22.5]$  Å compared to ceramic and polymer far from the surface, which again is a strikingly different result than for the other systems. This region coincides with the  $\text{Li}^+$  depletion region observed in the density profile at the L-LLZO surface (Fig. 8a). If combining the analysis of survival probabilities and density profiles, a distinctive mode of transport at the L-LLZO side can be observed in the vdW-LiZrO system, which is not present in the vdW-UFF simulations. The depletion region seen in Fig. 8a in region  $[-27.0, -22.0]$  Å in the vdW-LiZrO system corresponds to an exceptionally quick decay of  $R(t)$ . This correlation indicates there are almost no stationary  $\text{Li}^+$  in this region, and the quick decay of  $R(t)$  suggests a flux of  $\text{Li}^+$  that pass through the polymer layer to reach the L-LLZO surface. A different mechanism is observed at the R-LLZO surface in the vdW-LiZrO system. Fig. 8b shows a pronounced peak in the region  $[22.0, 27.0]$  Å which is also characterised by a high survival probability (Fig. 3). This means that the  $\text{Li}_{\text{PEO}}^+$  at the R-LLZO side are fairly stationary. The flux of  $\text{Li}^+$  can still occur, but on a significantly longer time scale.

Comparing non-bonded potentials in the vdW-UFF and vdW-LiZrO systems shows that irrespective of the atom pair, the difference between the potentials becomes negligible above 3 Å and in many cases above 2.5–3 Å. However, in the region below that, the discrepancy between the interaction energies increases significantly. For example, the  $C_{\text{PEO}}\text{--}O_{\text{LLZO}}$  pair interaction energy difference between the vdW-UFF and vdW-LiZrO systems at about 2 Å is equal to  $70 \text{ kJ mol}_{\text{pair}}^{-1}$ , while for the  $O_{\text{PEO}}\text{--}\text{Li}^+$  pair it is equal to  $10 \text{ kJ mol}_{\text{pair}}^{-1}$ . The interaction analysis suggests that the  $\text{Li}^+$  migration properties at the interface are very sensitive to the choice of vdW cross integration parameters. While the actual variation of the interaction energy is only pronounced up to 3 Å from an atom, this still renders a

noticeable impact on the density profiles, survival probabilities and on the mode of  $\text{Li}^+$  transport perpendicular to the surface.

## 4 Conclusions

In this study, classical molecular dynamics simulations were used in order to investigate the static and dynamic properties of a ceramic–polymer interface comprising PEO-based polymer electrolyte and cubic LLZO ceramic phases. The aim was to assess the influence of several model parameters on the simulation outcome, and was evaluated by how density profiles and survival probabilities are affected by the atomic partial charges, vdW cross interactions, polymer chain length and LLZO surface termination.

There are three main conclusions made from this study: (i) structural effects, in particular surface terminations, have a significant impact on the interfacial atomic arrangements in both polymer and ceramic phases. This was clearly seen from the distinct differences in the atomic density profiles between the two LLZO surfaces, and the fact that  $\text{Li}_{\text{PEO}}^+$  enters the ceramic phase only through the left surface terminated with oxygen. (ii) Force field effects, especially van der Waals cross phase interactions modify the mode of  $\text{Li}^+$  transport at the interface. (iii) Independent of the simulation setup, the inter-phase regions stretch across the same distance perpendicular to the LLZO surfaces. This is reflected in atomic density profiles and survival probabilities which are modified compared to the bulk-like regions. The distance that is affected by the existence of the interface, for any of the studied structure–dynamic properties, spans about 15 Å and about 11 Å from the LLZO surface in the PEO and LLZO phase respectively. This suggests that even without a perfectly optimised force-field, we may still draw some conclusions about  $\text{Li}^+$  mobility at the PEO/LLZO interface.

The complexity of these composite systems makes it challenging to systematically check every aspect of importance for the model. For this reason, the analysis here consists of a limited number of setups, targeting the exploration of the sensitivity of certain simulation parameters. This certainly does not exhaust the topic of important aspects that should be verified before a more definite picture of  $\text{Li}^+$  transport phenomena in the composite material can be provided. For example, the present study has only examined the surface with one orientation, and one surface cleavage. It is thereby still not clear to what extent these findings can be generalised with respect to different surface orientations and terminations.

The picture of  $\text{Li}^+$  transport in the PEO–LLZO composite material is still far from understood, and the molecular dynamics simulations described here primarily demonstrate that certain aspects of the simulation setup can significantly affect the outcomes of the study. It is crucial to highlight that, while this paper does not aim to determine realistic details regarding  $\text{Li}^+$  transport phenomena at the interface, we are actively exploring the most suitable setup to address the remaining physical questions related to lithium mobility in this category of electrolytes. In this context, the results of this



study constitute a step forward towards more accurate and reproducible simulations of ceramic–polymer interfaces, which is particularly relevant in the field of all solid-state batteries.

## Author contributions

Melania Kozdra: conceptualization, investigation, writing – original draft; Daniel Brandell: conceptualization, supervision, resources, writing – original draft, funding acquisition; Carlos Moyses Araujo: conceptualization, supervision, funding acquisition; Amber Mace: conceptualization, methodology, writing – original draft, supervision, funding acquisition.

## Conflicts of interest

There are no conflicts to declare.

## Acknowledgements

The authors thank the Swedish Energy Agency (project 50098-1), Swedish Research Council (Registration No. 2019-05366 and 2020-05223), and STandUP for Energy and Swedish National Strategic e-Science programme (eSSSENCE) for the financial support. The calculations were performed on resources provided by the National Academic Infrastructure for Supercomputing in Sweden (NAISS) at PDC.

## Notes and references

- 1 J. Janek and W. G. Zeier, *Nat. Energy*, 2023, **8**, 230–240.
- 2 A.-G. Nguyen and C.-J. Park, *J. Membr. Sci.*, 2023, **675**, 121552.
- 3 J. Zheng and Y. Y. Hu, *ACS Appl. Mater. Interfaces*, 2018, **10**, 4113–4120.
- 4 J. Zagórski, J. M. López Del Amo, M. J. Cordill, F. Aguesse, L. Buannic and A. Llordés, *ACS Appl. Energy Mater.*, 2019, **2**, 1734–1746.
- 5 W. Zhang, K. S. Kjær, R. Alonso-Mori, U. Bergmann, M. Chollet, L. A. Fredin, R. G. Hadt, R. W. Hartsock, T. Harlang, T. Kroll, K. Kubiček, H. T. Lemke, H. W. Liang, Y. Liu, M. M. Nielsen, P. Persson, J. S. Robinson, E. I. Solomon, Z. Sun, D. Sokaras, T. B. Van Driel, T. C. Weng, D. Zhu, K. Wärnmark, V. Sundström and K. J. Gaffney, *Chem. Sci.*, 2016, **8**, 515–523.
- 6 W. Li, C. Sun, J. Jin, Y. Li, C. Chen and Z. Wen, *J. Mater. Chem. A*, 2019, **7**, 27304–27312.
- 7 W. Wiczeorek, Z. Florjanczyk and J. R. Stevens, *Electrochim. Acta*, 1995, **40**, 2251–2258.
- 8 J. Zheng, M. Tang and Y.-Y. Hu, *Angew. Chem.*, 2016, **128**, 12726–12730.
- 9 Z. Li, H. M. Huang, J. K. Zhu, J. F. Wu, H. Yang, L. Wei and X. Guo, *ACS Appl. Mater. Interfaces*, 2019, **11**, 784–791.
- 10 J. Fu, Z. Li, X. Zhou and X. Guo, *Mater. Adv.*, 2022, **3**, 3809–3819.
- 11 J. Zheng and Y. Y. Hu, *ACS Appl. Mater. Interfaces*, 2018, **10**, 4113–4120.
- 12 J. Zhang, N. Zhao, M. Zhang, Y. Li, P. K. Chu, X. Guo, Z. Di, X. Wang and H. Li, *Nano Energy*, 2016, **28**, 447–454.
- 13 X. Peng, K. Huang, S. Song, F. Wu, Y. Xiang and X. Zhang, *ChemElectroChem*, 2020, **7**, 2389–2394.
- 14 Z. Wan, D. Lei, W. Yang, C. Liu, K. Shi, X. Hao, L. Shen, W. Lv, B. Li, Q. H. Yang, F. Kang and Y. B. He, *Adv. Funct. Mater.*, 2019, **29**, 1805301.
- 15 D. Brogioli, F. Langer, R. Kun and F. La Mantia, *ACS Appl. Mater. Interfaces*, 2019, **11**, 11999–12007.
- 16 M. R. Bonilla, F. A. García Daza, P. Ranque, F. Aguesse, J. Carrasco and E. Akhmatkaya, *ACS Appl. Mater. Interfaces*, 2021, **13**, 30653–30667.
- 17 M. R. Bonilla, F. A. García Daza, H. A. Cortés, J. Carrasco and E. Akhmatkaya, *J. Colloid Interface Sci.*, 2022, **623**, 870–882.
- 18 T. A. Manz and N. G. Limas, *RSC Adv.*, 2016, **6**, 47771–47801.
- 19 C. Campaña, B. Mussard and T. K. Woo, *J. Chem. Theory Comput.*, 2009, **5**, 2866–2878.
- 20 R. Jalem, M. J. Rushton, W. Manalastas, M. Nakayama, T. Kasuga, J. A. Kilner and R. W. Grimes, *Chem. Mater.*, 2015, **27**, 2821–2831.
- 21 G. Bergerhoff, I. Brown and F. Allen, *Int. Union Crystallogr., Crystallogr. Symp.*, 1987, **360**, 77–95.
- 22 H. Xie, J. A. Alonso, Y. Li, M. T. Fernández-Díaz and J. B. Goodenough, *Chem. Mater.*, 2011, **23**, 3587–3589.
- 23 W. Sun and G. Ceder, *Surf. Sci.*, 2013, **617**, 53–59.
- 24 R. Tran, Z. Xu, B. Radhakrishnan, D. Winston, W. Sun, K. A. Persson and S. P. Ong, *Sci. Data*, 2016, **3**, 160080.
- 25 T. Thompson, S. Yu, L. Williams, R. D. Schmidt, R. GarciaMendez, J. Wolfenstine, J. L. Allen, E. Kioupakis, D. J. Siegel and J. Sakamoto, *ACS Energy Lett.*, 2017, **2**, 462–468.
- 26 A. Padua, K. Goloviznina and Z. Gong, *ffttool v1.2.1*, DOI: [10.5281/zenodo.593728](https://doi.org/10.5281/zenodo.593728).
- 27 P. J. in't Veld and G. C. Rutledge, *Macromolecules*, 2003, **36**, 7358–7365.
- 28 A. I. Jewett, D. Stelter, J. Lambert, S. M. Saladi, O. M. Roscioni, M. Ricci, L. Autin, M. Maritan, S. M. Bashusqeh, T. Keyes, R. T. Dame, J.-E. Shea, G. J. Jensen and D. S. Goodsell, *J. Mol. Biol.*, 2021, **433**, 166841.
- 29 A. P. Thompson, H. M. Aktulga, R. Berger, D. S. Bolintineanu, W. M. Brown, P. S. Crozier, P. J. in't Veld, A. Kohlmeyer, S. G. Moore, T. D. Nguyen, R. Shan, M. J. Stevens, J. Tranchida, C. Trott and S. J. Plimpton, *Comput. Phys. Commun.*, 2022, **271**, 108171.
- 30 W. L. Jorgensen, D. S. Maxwell and J. Tirado-Rives, *J. Am. Chem. Soc.*, 1996, **118**, 11225–11236.
- 31 J. N. Lopes and A. A. Pádua, *J. Phys. Chem. B*, 2004, **108**, 16893–16898.
- 32 H. Wu and C. D. Wick, *Macromolecules*, 2010, **43**, 3502–3510.
- 33 L. R. Martins, M. S. Skaf and B. M. Ladanyi, *J. Phys. Chem. B*, 2004, **108**, 19687–19697.
- 34 G. S. Larsen, P. Lin, K. E. Hart and C. M. Colina, *Macromolecules*, 2011, **44**, 6944–6951.
- 35 P. Liu, E. Harder and B. J. Berne, *J. Phys. Chem. B*, 2004, **108**, 6595–6602.





- 36 M. Ebadi, L. T. Costa, C. M. Araujo and D. Brandell, *Electrochim. Acta*, 2017, **234**, 43–51.
- 37 A. Thum, D. Diddens and A. Heuer, *J. Phys. Chem. C*, 2021, **125**, 25392–25403.
- 38 D. J. Brooks, B. V. Merinov, W. A. Goddard, B. Kozinsky and J. Mailoa, *Macromolecules*, 2018, **51**, 8987–8995.
- 39 R. Jalem, Y. Yamamoto, H. Shiiba, M. Nakayama, H. Munakata, T. Kasuga and K. Kanamura, *Chem. Mater.*, 2013, **25**, 425–430.

